


Active hydrothermal fluids circulation triggering small-scale collapse events: the case of the 2001–2002 fissure in the Lakki Plain (Nisyros Island, Aegean Sea, Greece)

Stefania Venturi^{1,2}  · Franco Tassi^{1,2} · Orlando Vaselli^{1,2} ·
Georges E. Vougioukalakis³ · Heba Rashed² · Christos Kanellopoulos⁴ ·
Chiara Caponi² · Francesco Capecchiacci^{1,2} · Jacopo Cabassi^{1,2} ·
Andrea Ricci⁵ · Luciano Giannini^{1,2}

Received: 3 January 2018 / Accepted: 9 April 2018 / Published online: 26 April 2018
© Springer Science+Business Media B.V., part of Springer Nature 2018

Abstract In 2001–2002, two ground collapses occurred in the island of Nisyros (Aegean Sea, Greece), which formed a 600 m long and up to 5 m wide fissure in the vegetated central part of the Lakki Plain caldera. The fissure was alternatively ascribed to tensional stress release and hydrothermal alteration. In this study, we present original data of diffuse CO₂ soil fluxes, soil temperatures, mineralogical and chemical composition of the caldera-filling deposits exposed on the fissure walls, and chemical and isotopic composition of interstitial soil gases collected from: the bottom of the fissure, the adjacent vegetated areas,

✉ Stefania Venturi
stefania.venturi@igg.cnr.it

Franco Tassi
franco.tassi@unifi.it

Orlando Vaselli
orlando.vaselli@unifi.it

Georges E. Vougioukalakis
gvoug@igme.gr

Heba Rashed
hebaafef.rashed@unifi.it

Christos Kanellopoulos
ckanellopoulos@gmail.com

Chiara Caponi
chiara.caponi@unifi.it

Francesco Capecchiacci
francesco.capecchiacci@unifi.it

Jacopo Cabassi
jacopo.cabassi@igg.cnr.it

Andrea Ricci
ricciandrea89@gmail.com

Luciano Giannini
luciano.giannini@gmail.com

the hydrothermal craters, and selected sites outside the caldera. The occurrence of intense hydrothermal alteration was shown by both mineralogical and chemical analyses of the fissure walls material. Typical mineral assemblage and enrichments in incompatible elements related to advanced argillic alteration, characterizing steam-heated hydrothermal environments, were recognized. Although the low-permeable sediment cover in the Lakki Plain concealed the underneath hydrothermal gas flow, preventing anomalous soil temperatures and CO₂ fluxes, the chemical and isotopic composition of the interstitial soil gases revealed an active hydrothermal fluids circulation below the collapsed area, likely controlled by buried structural lineaments. Hydrothermal alteration can then be invoked as the most likely trigger mechanism for the 2001–2002 collapse event.

Keywords Ground collapse · Hydrothermal alteration · Fissuring · Nisyros Island · Volcanic-hydrothermal systems · Hydrothermal fluid circulation

1 Introduction

Small-scale collapse events widely occur at the Earth surface in diverse geological contexts posing risks to humans, animals, and infrastructures, especially when they occur with no precursory signals (e.g., Waltham and Fookes 2003; Waltham et al. 2005). In sedimentary basins, ground depressions (e.g., sinkholes, dolines) commonly form in karst landscapes, due to the dissolution of soluble rocks (such as limestone, dolomite or gypsum) and/or groundwater level changes (after drought or, conversely, heavy rains; e.g., Caramanna et al. 2008; Linares et al. 2017). Human activities (e.g., mining, excessive groundwater pumping, oil and gas extraction from underground reservoirs) may also trigger ground collapses (e.g., Waltham et al. 2005; Gutiérrez et al. 2014). In geodynamically active areas, tensional stresses associated with tectonic or magmatic activity or hydrothermal fluid pressurization (e.g., Heidari et al. 2011; Santo et al. 2011; Billi et al. 2016) can be enumerated among ground fissuring causes. In geothermal areas, circulation of hydrothermal fluids typically characterized by high contents of acidic gases (CO₂ and H₂S) is responsible of strong alteration of surficial terrains, causing hypogenic dissolution and, consequently, hydrothermal karstification (López and Williams 1993; Bosák 2000; Dublyansky 2000; Caramanna et al. 2008; Dublyansky 2013; Frumkin et al. 2015; Rosas-Carbajal et al. 2016). This upward weathering, mainly occurring through vertical conduits (faults and fractures) that favor the uprising of the hydrothermal fluids, may trigger soil collapse phenomena.

At Nisyros Island, a Quaternary stratovolcano located in the Dodecanese (SE Aegean Sea, Greece), a soil collapse occurred in 2001–2002, producing a 600 m long and up to

¹ Institute of Geosciences and Earth Resources of the National Research Council of Italy (IGG-CNR), Via G. La Pira 4, 50121 Florence, Italy

² Department of Earth Sciences, University of Florence, Via G. La Pira 4, 50121 Florence, Italy

³ Institute of Geology and Mineral Exploration, S. Lui 1, Olympic Village, Acharne, 13677 Athens, Greece

⁴ Department of Geology and Geoenvironment, National and Kapodistrian University of Athens, Panepistimioupoli Zografou, 15784 Athens, Greece

⁵ Department of Biological, Geological and Environmental Sciences, University of Bologna, Porta S. Donato 1, Bologna, Italy

5 m wide fissure in a vegetated portion of the Lakki Plain caldera. Different mechanisms were invoked to explain this event, such as: (1) uncompensated stress conditions (horizontal tensional forces) in the near surface after the 1996–1998 seismic crisis (Lagios et al. 2005) and (2) unusually high precipitation rate that saturates the soil with possible collapses into preexisting zones of soil weakness (Vougioukalakis 2003; Vougioukalakis and Fytikas 2005). The latter has tentatively been referred to hypogenic hydrothermal alteration (Vanderkluyzen and Gex 2005; Volentik et al. 2005b), similar to the holes produced on the floor of Stephanos crater (about 1 km away from the fissure) in wintertime. However, this explanation was only based on the interpretation of field observations as no data or field measurements were produced to support this hypothesis. Thus, the cause(s) of this collapse episode is still matter of discussion.

In this paper, we evidenced the presence of hydrothermal alteration of the shallow caldera-filling terrains exposed on the fissure walls through chemical and mineralogical analyses. Furthermore, the chemical and isotopic ($\delta^{13}\text{C}$ in CO_2) composition of interstitial soil gases from the (1) fissure bottom, (2) adjacent areas in the Lakki Plain, (3) hydrothermal craters, (4) hydrothermally altered terrains of the caldera, and (5) outer border of the caldera revealed the occurrence of active hydrothermal fluids circulation underneath the collapsed area.

2 Geological settings and hydrothermal activity in the study area

Nisyros is the easternmost Quaternary volcano of the so-called South Aegean Active Volcanic Arc (SAAVA), whose activity is related to the subduction of the African continental crust beneath the Aegean–Anatolian plate (Francalanci et al. 2005; Pe-Piper and Piper 2005). The SAAVA extends from Methana peninsula westward, to Milos, Santorini, and Kolumbo in its central part, and Nisyros, Yali, and Kos close to the Anatolian coast (Fig. 1a). Nisyros is built up on a Mesozoic limestone and Neogene sedimentary basement. Volcanic products mainly consist of basaltic and andesitic lavas, pumice fall deposits, pyroclastic layers, and rhyodacitic domes (e.g., Francalanci et al. 1995; Vanderkluyzen et al. 2005; Volentik et al. 2005a; Tibaldi et al. 2008). The last eruption occurred at least 25 ka BP (Hurni et al. 2005). The island currently has a truncated cone shape, with a base diameter of 8 km and a surface area of about 42 km². The 4 km in diameter Lakki Plain caldera formed < 20 ka, after a major collapse of the volcanic edifice (Tibaldi et al. 2008 and references therein).

The southern portion of the Lakki Plain was affected by several phreatic explosions producing a series of hydrothermal craters (Fig. 1b–d), the most recent ones being occurred in the nineteenth century (1871–1873 and 1888; e.g., Marini et al. 1993 and references therein). This area shows a relatively vigorous fumarolic activity, high soil diffuse degassing, thermal anomalies and intensely hydrothermalized barren terrains (Fig. 1b–d) related to the presence of an active high-temperature hydrothermal system (e.g., Chiadini et al. 2002; Cardellini et al. 2003; Caliro et al. 2005; Marini and Fiebig 2005; Ambrosio et al. 2010). Direct information on the stratigraphy and on the hydrothermal system was retrieved from two deep geothermal wells (Nis-1 and Nis-2) drilled in the southern part of the Lakki Plain (Geotermica Italiana 1983, 1984). The terrains encountered by the two wells consisted of (1) alluvial, lacustrine, and tephra deposits up to 600 and 1000 m thick in Nis-1 and Nis-2, respectively, (2) carbonate rocks, found at > 1000 m depth in Nis-1 and not present in Nis-2, and (3) diorites with associated thermometamorphic rocks at

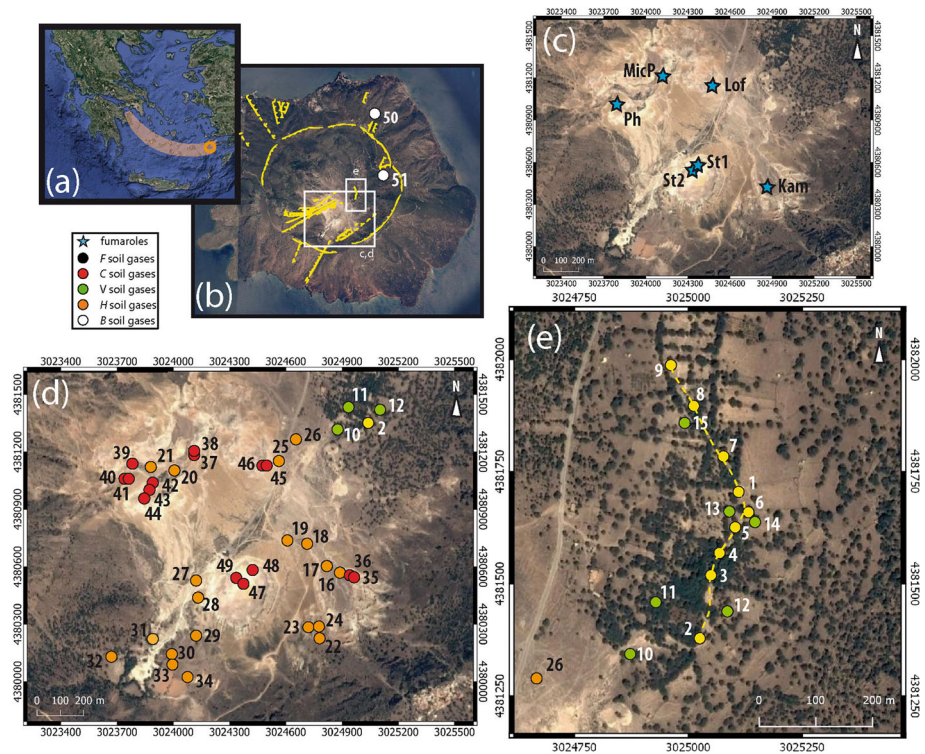


Fig. 1 **a** Location map and **b** satellite image of Nisyros Island. In **a**, the transparent orange area identifies the SAAVA, whereas the orange circle indicates the location of Nisyros Island. In **b**, the caldera rim is reported together with main faults (yellow lines), while the white squares identify the areas zoomed in **c–e**. The location of *F* (yellow circles), *C* (red circles), *V* (green circles), *H* (orange circles), *B* (white circles) sites and the sampled fumarolic vents (blue stars) are reported. In **(e)**, the location of the fissure is reported (yellow dashed line)

1816 m in Nis-1 and underneath the sedimentary-volcanic series in Nis-2. Two hydrothermal reservoirs were recognized, as follows: (1) at 431–695 and 30–365 m depth in Nis-1 and Nis-2, respectively, where temperatures up to 180 °C were measured; (2) at 1421–1816 m depth in Nis-1 and at 1070–1360 m depth in Nis-2, with temperatures up to 340 °C (Geotermica Italiana 1983, 1984; Brombach et al. 2003; Caliro et al. 2005; Ambrosio et al. 2010). NE–SW-elongated tectonic structures, associated with a main E–W extension (Tibaldi et al. 2008), play a major role in controlling the hydrothermal fluids upflow toward the surface, as indicated by both the location of the hydrothermal craters (Caliro et al. 2005) and the corresponding CO₂ flux anomalies (Brombach et al. 2001, 2003). Moreover, the circulating hydrothermal fluids feed several thermal springs located in the northern and southern coasts of the island, though strongly affected by seawater (Chiodini et al. 1993; Brombach et al. 2003; Ambrosio et al. 2010).

3 The 2001–2002 fissure

On November 20, 2001 a SSW–NNE-oriented 350 m long and 1–5 m wide fissure opened overnight, without any precursory signals, in the vegetated central part of the Lakki Plain (Figs. 1e, 2). On December 18, 2002, a second collapse event occurred, extending 250 m southward the fissure, whose maximum depth was up to 15–20 m. Neither vertical shifts of the ground surface nor visible gas release nor seismic signals (Lagios et al. 2005) were observed during the rupturing event. Notwithstanding, it is worth mentioning that the fissuring of the caldera floor chronologically followed the seismic crisis that affected Nisyros in 1996–1998 (Papadopoulos et al. 1998), which was accompanied by ground deformation (Lagios et al. 2005) and significant compositional changes of the fumarolic gases (Chiodini et al. 2002), raising concerns on possible volcanic activities (Kinvig et al. 2010). The relatively short temporal interval of the two collapsing events allowed Lagios et al. (2005) to suggest that horizontal tensional forces related to the 1996–1998 unrest produced the fissuring event as a consequence of stress release at the near surface. However, no significant changes in the seismic and hydrothermal activity were recorded immediately before, during or after the fissure opening as well as no signs of horizontal displacements along the fissure were detected. Other authors (Vougioukalakis 2003; Vougioukalakis and Fytikas 2005) hypothesized that the rupture was produced by a passive collapse of the upper, < 50 m thick caldera floor sediment cover into the lower, highly permeable open framework, coarse caldera deposits. This mechanism was likely favored and triggered by anomalous heavy rains that affected Nisyros during winter 2001, along tectonic lineaments reactivated during the 1996–1998 seismic crisis and possibly affected

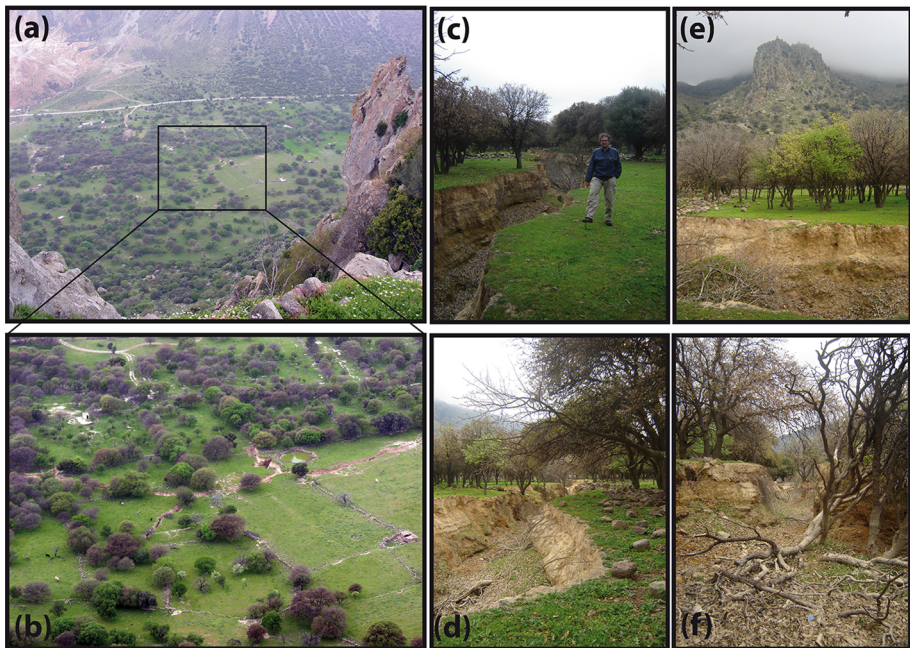


Fig. 2 Photographs of the 2001–2002 fissure, i.e., **a** general view of the 2001–2002 fissure from the eastern wall of the Nisyros caldera; **b** detail of the 2001–2002 fissure; **c–f** images of the 2001–2002 fissure taken from different sites

by intense hydrothermal fluid circulation. On the basis of geophysical data, Vanderkluyssen and Gex (2005) and Volentik et al. (2005b) suggested that the ground collapse occurred where acidic fluids from the crater area, driven by preexisting local faults, were present resulting in a more efficient soil chemical alteration. This mechanism seemed to be consistent with the available CO₂ soil flux measurements carried out in the Lakki Plain, which showed the occurrence of NE-SW oriented DDS (Diffuse Degassing Structures) (Brombach et al. 2001; Caliro et al. 2005).

4 Methods and materials

4.1 Sampling and analyses of fissure wall deposits

Soil samples from three selected sites on the fissure walls (LF-1, LF-2, and LF-3; Fig. 3) were collected in polyethylene bags. The samples were dried at 40 °C and grinded with a planetary agate ball mill to obtain an impalpable powder. The main mineralogical composition was determined at the Department of Earth Sciences at University of Florence by powder X-ray diffraction (XRD), using a Philips PW 1050/37 diffractometer equipped with a Philips X'Pert data acquiring system. The diffractometer operated at 40 kV–20 mA, Cu anticathode, graphite monochromator, 2°/min goniometry speed, scanning range 2θ between 5°–70°, with a detection limit of 4 wt%. Total volatile components were determined as loss on ignition (L.O.I.) by gravimetry. About 1 g of powdered sample was dried at 110 °C for 8 h, weighted into quartz–fiber crucibles, and then heated at 950 °C for 2 h using a CEM microwave oven. The L.O.I. (in %) was calculated as weight loss after heating, as follows:

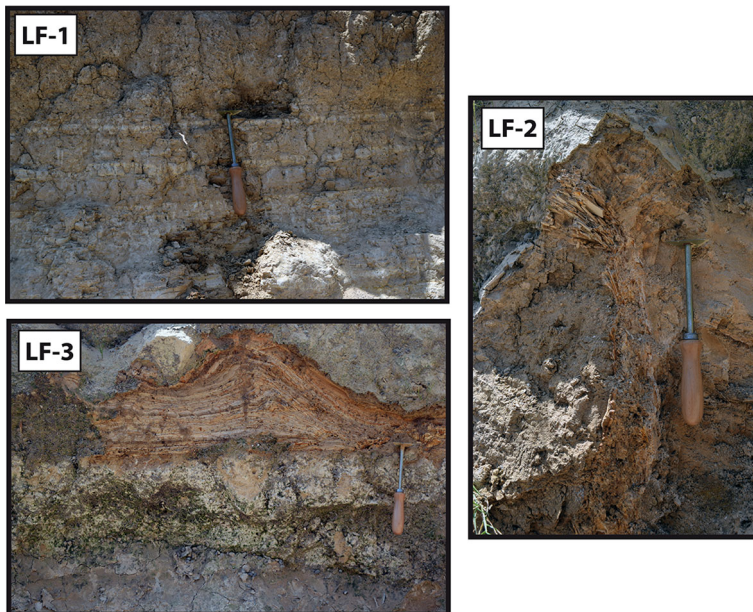


Fig. 3 Photographs of sites (LF-1, LF-2 and LF-3) where fissure wall deposits were collected

$$\text{L.O.I.} = \frac{W_i - W_f}{W_i - W_c} \times 100, \quad (1)$$

where W_i is the initial weight (in grams) of the crucible containing the 1 g dry powder, W_f is the final weight (in grams) of the crucible containing the ignited dry powder, and W_c is the weight (in grams) of the crucible. The bulk-soil chemical composition was analyzed by X-ray fluorescence (XRF) on pressed powder pellets, using a Rigaku II wavelength-dispersive spectrometer equipped with a Rh anode at CRIST (Center of Structural Crystallography—University of Florence). The composition of the main and trace elements was acquired using a ZSX Rigaku Software Package version 3.50 and determined with the SQX semiquantitative element analysis routine. The Fundamental Parameter (FP) software was used to allow elemental quantification of the samples.

4.2 CO₂ soil flux measurements

The CO₂ soil fluxes (ΦCO_2) were measured in June 2015 from 51 sites (Fig. 1b–e) located at (1) the fissure bottom (F ; sites #1 to #9), (2) the adjacent vegetated areas in the Lakki Plain (V ; sites #10 to #15), (3) the hydrothermally altered portion of the Lakki Plain (H ; sites #16 to #34), (4) several craters created by hydrothermal explosions (C ; sites #35 to #49), and (5) the margins of the caldera (B ; sites #50 and #51) by the “accumulation chamber (AC) method” (Chiodini et al. 1998). The measuring apparatus consisted of: (1) a cylindrical metal chamber (basal area: 200 cm²; inner volume: 3060 cm³), (2) an infrared (IR) spectrophotometer Licor[®] Li-820 (measuring range 0–20,000 ppm; accuracy: 4%), (3) an analog-to-digital (AD) converter, and (4) a palmtop computer equipped with Palm Flux 5.36 software (Tassi et al. 2015). The chamber was placed on the ground and a low-flux pump (operating at 20 mL/s) allowed to continuously (1) convey the gas from the chamber to the IR spectrophotometer and (2) reinject the gas into the chamber. The concentrations of CO₂ inside the chamber, continuously measured by the IR spectrophotometer, were acquired by the AD converter and visualized on the palmtop. The ΦCO_2 value, expressed in g m⁻² d⁻¹, was computed, as follows:

$$\Phi\text{CO}_2 = cf \times d\text{CO}_2/dt, \quad (2)$$

where dC_{CO_2}/dt (expressed in ppm s⁻¹) is the initial slope of the CO₂ concentration versus time curve, and cf is a proportionality factor determined by laboratory tests, which depends on (1) the geometry of the measuring apparatus, (2) the air pressure, and (3) the air temperature (Chiodini et al. 1998).

4.3 Sampling and analyses of interstitial soil gases

Interstitial soil gases were collected in the same sites where the CO₂ soil flux measurements were carried out (F , V , H , C and B ; Fig. 1b–e). The sampling apparatus consisted of (1) a stainless-steel tube inserted down to the sampling depth (20 and 40 cm depth, with the exception of four sampling sites, i.e., #37, #38, #45 and #46, where the soil hardness allowed to reach 20 cm depth only), (2) a PTFE three-way valve, to connect the tube to (3) a 12 mL glass vial equipped with a pierceable rubber septum (Labco Exetainer[®]), and (4) a 60 mL plastic syringe to pump the interstitial gases from the tube to the vial (Tassi et al. 2015). Soil temperatures were measured using a LT Lutron four-channel thermometer equipped with a K-type thermocouple (range – 50.0 to 999.9 °C; accuracy: ± 0.4% + 0.5 °C).

Fumarolic gases from six fluid discharges located in Phlegethon, Kaminakia, Stephanos, and Polybotes Micros craters and Lofos dome (Fig. 1c) were collected using a titanium tube inserted into the fumarolic vent. The tube was connected to a sampling line consisting of dewared glass tubes conveying the gas into a pre-evacuated 60 mL glass flask, equipped with a Thorion[®] valve, containing a 4 M NaOH and 0.15 M Cd(OH)₂ suspension (Montegrossi et al. 2001). Two aliquots of dry gas samples for the analysis of (1) volatile organic compounds (VOCs) and (2) $\delta^{13}\text{C}\text{-CO}_2$, respectively, were collected into 12 mL Labco Exetainer[®] glass vials after water vapor condensation via a Graham-type condenser connected to the dewared glass line (Tassi et al. 2012, 2015). The outlet temperatures of the fumaroles were measured using the LT Lutron thermometer.

Nitrogen, O₂, Ar, and H₂ were analyzed by a Shimadzu 15A gas chromatograph (GC) equipped with a thermal conductivity detector (TCD) and a 10 m long 5A Molecular Sieve column. Carbon dioxide and H₂S in the interstitial soil gases were analyzed using the same GC equipped with a 3 m long column filled with Porapak Q (80/100 mesh). The analysis of light hydrocarbons (C₁–C₃) was performed using a Shimadzu 14A GC equipped with a flame ionization detector (FID) and a 10 m long stainless-steel column filled with 23% SP 1700 on Chromosorb PAW (80/100 mesh). Carbon dioxide and H₂S, trapped into the alkaline solution of the sampling flasks (as CO₃²⁻ and SO₄²⁻, respectively), were analyzed by automatic titration (AT; Metrohm 794 Basic Titrino) using a 0.5 M HCl solution, and ionic chromatography (IC; Metrohm 761 Compact) after oxidation with H₂O₂, respectively (Montegrossi et al. 2001; Vaselli et al. 2006).

In order to analyze C₄₊ VOCs in fumarolic and soil gases, gas samples in the glass vials were exposed to a 2 cm long DiVinylBenzene—Carboxen—PolyDiMethylSiloxane fiber (Supelco; Bellefonte, PA, USA) for 30 min at 20 °C (Solid Phase Micro Extraction, SPME; Arthur and Pawliszin 1990; Tassi et al. 2012, 2015). VOCs trapped by the SPME fiber were desorbed for 2 min at 230 °C in the column headspace of a Thermo Trace GC Ultra coupled with a Thermo DSQ quadrupole mass spectrometer (MS), and injected through a split/splitless port equipped with a SPME liner (0.75 mm inner diameter) into a TR-V1 fused silica capillary column (Thermo; 30 m length × 0.25 mm inner diameter, 1.4 μm film thickness). Helium was used as carrier gas in constant pressure mode at a flow rate of 1.3 mL/min. The column oven temperature was set at 35 °C for 10 min and then increased first (1) with a ramp-up rate of 5.5 °C/min to 180 °C, where it was held for 3 min, and then (2) with a ramp-up rate of 20 °C/min to 230 °C, where it was held for 6 min (Tassi et al. 2012, 2015). After chromatographic separation, gases passed, through a transfer-line set at 230 °C, to the MS operating under the following conditions: positive electron impact mode (EI), ionization energy of 70 eV, source temperature of 250 °C, and quadrupole detector in full -can mode operating in the mass range 35–400 m/z (Tassi et al. 2015). Both retention times of the analytes and their mass spectra were used to identify VOCs by comparison with the mass spectra database of the NIST05 library (NIST 2005). Quantitative analyses were carried out by external standard calibration procedure, using AccuStandard[®] mixtures in methanol or hexane solvent, as described by Tassi et al. (2012, 2015 and references therein). Analytical errors for AT, IC, and GC were < 5%.

The carbon isotopic composition of CO₂ (expressed as $\delta^{13}\text{C}\text{-CO}_2$ ‰ vs. V-PDB) was determined by using a Finningan MAT252 MS at CNR-IGG (Pisa) after a two-step extraction and purification procedure of the gas mixtures by using liquid N₂ and a solid-liquid mixture of liquid N₂ and trichloroethylene (Evans et al. 1998; Vaselli et al. 2006) at the Department of Earth Sciences at University of Florence. External precision was estimated using internal (Carrara and San Vincenzo marbles) and international (NBS18 and

NBS19) standards. The analytical uncertainty and the reproducibility were ± 0.05 and $\pm 0.1\%$, respectively.

5 Results

5.1 Mineralogical and bulk chemical composition of fissure wall deposits

The mineralogical composition of the fissure walls was dominated by the presence of silicates, i.e., albite, quartz, and nontronite (Fe-rich smectite), and sulfate minerals, i.e., natroalunite, jarosite, and barite (Table 1).

The concentrations of major (expressed in wt%) and trace elements (expressed in ppm) by XRF are reported in Table 2. The most abundant element was SiO₂, which ranged from 59.10 to 65.08 wt%, followed by Al₂O₃ (from 4.84 to 15.64 wt%), Fe₂O₃ (from 6.21 to 10.58 wt%), consistent with the presence of albite, quartz, and nontronite. Loss on ignition values ranged from 7.1 up to 10.8 wt%. K₂O, MgO, CaO, and Na₂O showed lower concentrations, ranging from 0.36 up to 2.86 wt%, while TiO₂, P₂O₅, and MnO were measured at concentrations varying from 0.01 to 0.71 wt%. Arsenic was only detected in LF-3 (0.47 wt%), where a relatively high concentration of Ba (3.63 wt%) compared to the other samples (≤ 0.14 wt%) was measured due to the presence of barite. S and Cl showed peculiarly high concentrations, ranging from 1.17 to 1.99 wt% and from 470 to 1200 ppm, respectively. Trace elements included Sr, Pb, and Zn, at concentrations ranging from 42 up to 971 ppm, while Zr, Cr, and V showed abundances from 122 to 217 ppm in LF-1 and LF-2 samples. Cu, Rb, Ni, Nb contents were up to 116 ppm.

5.2 CO₂ soil flux measurements

The Φ CO₂ values (Table 3) measured in the *F* sites ranged from 1.23 to 28.5 g m⁻² d⁻¹. These fluxes, slightly higher than those measured both in the *B* (≤ 0.43 g m⁻² d⁻¹) and *V* (from 0.03 to 5.79 g m⁻² d⁻¹) sites, were in the same range of those measured in the hydrothermally altered area of the Lakki Plain (*H* sites; from 0.14 to 28 g m⁻² d⁻¹). As expected, the CO₂ fluxes measured within the hydrothermal craters (*C* sites; from 10.3 to 208 g m⁻² d⁻¹) were up to one order of magnitude higher than the other sites.

Table 1 Mineralogical composition of fissure wall deposits resulted from XRD analysis

Mineral	Formula	LF1	LF2	LF3
Albite, ordered	NaAlSi ₃ O ₈			x
Albite, disordered	Na(Si ₃ Al)O ₈	x	x	
Quartz	SiO ₂	x	x	x
Nontronite	Na _{0.3} Fe ₂ Si ₄ O ₁₀ (OH) ₂ × 4H ₂ O	x	x	x
Jarosite	KFe ₃ (SO ₄) ₂ (OH) ₆	x		
Natroalunite	NaAl ₃ (SO ₄) ₂ (OH) ₆	x	x	x
Barite	BaSO ₄			x

Table 2 Bulk geochemistry of major (in wt%), minor and trace (in ppm) elements of fissure wall deposits. The L.O.I. (loss on ignition) values (in wt%) are also shown

	LF-1	LF-2	LF-3
SiO ₂ (wt%)	59.10	59.38	65.08
TiO ₂ (wt%)	0.68	0.71	0.32
Al ₂ O ₃ (wt%)	14.21	15.64	4.84
Fe ₂ O ₃ (wt%)	6.22	6.21	10.58
MnO (wt%)	0.05	0.07	0.01
MgO (wt%)	2.08	2.80	0.42
CaO (wt%)	2.06	2.86	0.36
K ₂ O (wt%)	2.42	2.25	0.78
Na ₂ O (wt%)	1.08	1.27	0.37
P ₂ O ₅ (wt%)	0.22	0.18	0.11
L.O.I (wt%)	9.50	7.10	10.80
S (wt%)	1.99	1.17	1.87
Ba (wt%)	0.14	0.10	3.63
As (wt%)	–	–	0.47
Cl (ppm)	470	500	1200
V (ppm)	122	167	–
Cr (ppm)	163	146	–
Ni (ppm)	50	64	47
Rb (ppm)	83	77	29
Sr (ppm)	437	447	971
Zr (ppm)	203	217	–
Nb (ppm)	20	–	–
Cu (ppm)	101	116	61
Pb (ppm)	373	276	743
Zn (ppm)	140	137	42

5.3 Soil temperature measurements

Soil temperatures at 20 and 40 cm depth varied from 19.9 to 97.9 °C and from 18.6 to 85.4 °C, respectively (Table 3). The highest values, showing increasing trends with depth, were measured in the craters (from 25.4 to 97.9 °C), followed by those of the *H* sites (from 21.9 to 41.3 °C). Decreasing trends with depth were shown in the *V* and *F* sites (up to 26.3 and 29.1 °C, respectively), as well as in the *B* sites (up to 30.5 °C).

5.4 Chemical and isotopic composition of soil gases

The chemical composition (in mmol/mol) of the main gas compounds of the interstitial soil gases is presented in Table 3. Nitrogen was by far the most abundant gas species, with concentrations up to 916 mmol/mol and 931 mmol/mol at 20 and 40 cm depth, respectively, with few exceptions, i.e., site #7 at 40 cm and site #38 at 20 cm, pertaining to groups *F* and *C*, respectively. The concentrations of CO₂ were inversely correlated with those of N₂ and ranged (1) from 2.9 to 418 mmol/mol and from 3.6 to 513 mmol/mol at 20 and 40 cm depth, respectively, in soil gases of type *F*, (2) from 1.4 to 31 mmol/mol and

Table 3 Soil temperature (in °C) and chemical composition of the main gas species (CO₂, H₂S, CH₄, N₂, O₂, Ar, H₂; in mmol/mol) and volatile organic compounds (in nmol/mol) in interstitial soil gases collected in sites 1 to 51 (a = 20 cm depth; b = 40 cm depth). The isotopic composition of CO₂ (δ¹³C-CO₂, in ‰ vs. V-PDB) and the ΦCO₂ values (in g m⁻² day⁻¹) measured at each sampling site are also reported. The sampling sites are classified into five groups according to their location

ID	Type	T	ΦCO ₂	CO ₂	H ₂ S	CH ₄	N ₂	O ₂	Ar	H ₂	C ₂ H ₆	C ₃ H ₈	n-C ₄ H ₁₀	i-C ₄ H ₈	C ₆ H ₆	C ₂ H ₆ S	C ₄ H ₄ S	δ ¹³ C-CO ₂
1a	F	29.1	4.4	156	1.10	0.31	815	21.0	6.70	0.12	178	15	2.1	13	21		0.9	
1b	F	24.7		169	1.30	0.39	822	0.31	6.90	0.13	295	28	3.8	21	36	0.4	2.1	- 6.8
2a	F	26.8	1.91	2.90		0.00	826	160	11.0		0.7							
2b	F	23.6		3.60		0.00	869	115	12.0		0.8							- 17.1
3a	F	19.9	8.38	12.0		0.00	887	90.0	11.0		1.50							
3b	F	18.6		215	0.70	0.11	776	0.65	7.50	0.04	150	12	1.8	9.1	14		0.7	- 10.8
4a	F	20.4	4.65	395	0.40	0.15	587	12.1	5.30	0.06	130	16	2.5	12	26		0.7	
4b	F	20.5		488	0.80	0.21	505	0.98	4.90	0.08	490	61	11	35	85	0.4	2.6	- 2.5
5a	F	26	28.5	104	0.20	0.11	825	63.0	7.80	0.04	54	6		3.1	6.1			
5b	F	20.1		109	0.70	0.11	872	10.0	7.90	0.04	130	15	2.3	11	22		0.7	- 3.1
6a	F	25	3.79	211	0.30	0.13	739	40.0	9.10	0.05	95	11	1.5	7.1	14			
6b	F	21.4		248	0.50	0.21	744	0.33	6.90	0.06	190	23	3.3	19	35		1.1	- 3.9
7a	F	24	3.7	418	0.20	0.22	575	0.89	5.60	0.09	160	18	3.1	13	23			
7b	F	21		513	0.90	0.38	480	0.11	5.50	0.11	390	46	8.5	32	66	0.4	2.1	- 3.1
8a	F	27.8	9.55	108	0.10	0.09	855	27.0	9.50	0.03	61	5.7	1.1	3.5	7.6			
8b	F	24.4		195	0.40	0.15	796	0.51	7.90	0.05	140	17	3.1	11	26		0.8	- 2.9
9a	F	24	1.23	2.90		0.00	839	147	11.0		0.9							
9b	F	23.1		3.60		0.00	857	128	11.0		1.6							- 16.1
35a	C	53	54.3	269	1.80	0.44	705	18.0	5.60	0.15	266	25	3.9	18	29		1.1	
35b	C	70		411	3.60	0.81	579	0.55	5.10	0.23	515	55	11	42	65	0.6	3.6	- 1.1
36a	C	33	64.9	171	0.90	0.33	802	19.0	7.10	0.11	231	22	3.1	17	25		0.8	
36b	C	41		295	1.60	0.71	695	1.30	6.30	0.21	537	57	11	44	63	0.6	3.5	- 1.4
37a	C	97.9	208	785	29.30	1.80	177	4.90	1.30	0.69	1450	160	33	130	210	1.1	7.5	- 1.1
38a	C	60.8	111	841	36.50	2.30	118	0.51	0.91	0.65	2380	270	55	220	350	3.1	19	- 0.9

Table 3 continued

ID	Type	T	ΦCO ₂	CO ₂	H ₂ S	CH ₄	N ₂	O ₂	Ar	H ₂	C ₂ H ₆	C ₃ H ₈	n-C ₄ H ₁₀	i-C ₄ H ₈	C ₆ H ₆	C ₂ H ₆ S	C ₄ H ₄ S	δ ¹³ C-CO ₂
39a	C	36.2	105	189		0.01	788	16.1	6.10		9	0.8			1.1			
39b	C	50.6		285		0.08	708	1.90	5.50	0.02	41	4.2		3.1	5.5			- 1.2
40a	C	32.6	11.4	25.0		0.02	891	73.0	11.0		6	0.5			0.6			
40b	C	34.9		51.0		0.04	906	31.0	12.0	0.01	29	2.6		1.5	3.5			- 4.9
41a	C	34	10.3	11.0		0.02	855	123	11.0		6	0.5			0.7			
41b	C	37.1		19.0		0.07	907	62.0	12.0		39	4.1		2.7	5.6			- 23.8
42a	C	38.9	40.6	41.0		0.08	896	51.0	12.0	0.02	81	8.5	1.4		11			
42b	C	48.3		66.0		0.15	921	0.82	12.0	0.03	130	15	2.7	11	19		0.6	- 6.7
43a	C	51.4	73.3	195		0.42	745	50.0	9.10	0.11	280	36	6.1	26	48	0.5	2.8	
43b	C	63.1		311		0.78	666	15.0	5.70	0.18	690	64	13	47	85	0.8	4.9	- 1.1
44a	C	56.7	72.2	136		0.23	811	45.0	7.30	0.06	180	21	3.5	16	33		1.5	
44b	C	66.4		256		0.65	733	1.90	7.10	0.12	660	85	15	59	120	1.1	7.1	- 1.4
45a	C	53	129	411		1.10	577	3.10	5.20	0.31	890	110	1.8	110	140	1.1	6.1	- 1.3
46a	C	47.5	74.0	355		0.60	637	0.46	5.70	0.29	1120	130	1.9		170	1.5	10	- 1.4
47a	C	25.4	27.1	16.0		0.30	872	101	11.0	0.11	41	4.1		2.4	6.9		0.5	
47b	C	25.9		39.0		0.12	905	43.0	12.0	0.13	150	17	3.1	13	23		1.3	- 2.6
48a	C	58.9	94.1	111		0.25	835	42.0	11.0	0.07	190	19	3.4	16	25		1.1	
48b	C	69.6		304		0.88	680	0.9	6.30	0.22	1260	150	28	120	210	1.9	12	- 1.1
49a	C	61.3	25.5	85.0		0.19	882	24.0	6.10	0.04	190	17	2.8	12	26		1.1	
49b	C	85.4		265		8.10	718	1.10	6.80	0.18	1440	180	35	150	250	2.5	14	- 1.0
10a	V	25	0.03	2.40		0.00	851	135	12.0		1.1							
10b	V	24		2.90		0.00	867	118	12.0		1.8							- 24.2
11a	V	22	5.79	1.40		0.00	833	155	11.0		0.5							
11b	V	21		1.90		0.00	844	142	12.0		0.6							- 21.8
12a	V	22.5	4.10	15.0		0.01	859	115	11.0		7.7	0.6						
12b	V	21.1		29.0		0.05	904	55.0	12.0		31	3.3						- 20.8

Table 3 continued

ID	Type	T	ΦCO ₂	CO ₂	H ₂ S	CH ₄	N ₂	O ₂	Ar	H ₂	C ₂ H ₆	C ₃ H ₈	n-C ₄ H ₁₀	i-C ₄ H ₈	C ₆ H ₆	C ₂ H ₆ S	C ₄ H ₄ S	δ ¹³ C-CO ₂
13a	V	26.3	2.05	3.60		0.00	844	141	11.0		0.5							-20.7
13b	V	21.5		3.90		0.00	877	108	11.0		0.5							
14a	V	24.5	4.88	31.0		0.01	891	67.0	11.0		3.1							
14b	V	23.6		51.0		0.02	911	26.0	12.0		11.0	1.1						-23.2
15a	V	25.3	0.92	2.80		0.00	843	143	11.0		0.5							
15b	V	22.1		2.70		0.00	869	117	11.0		0.5							-23.1
16a	H	34.3	12.3	36.0		0.01	904.45	49.97	9.59		3.6	0.5						
16b	H	33.2		48.0		0.01	912.08	30.00	9.90		5.1	0.5						-12.5
17a	H	34	12.8	11.0		0.00	879.00	99.00	11.00		1.5							
17b	H	35.6		12.0		0.01	901.99	74.00	12.00		2.6							-18.6
18a	H	37.2	4.14	10.0		0.00	888.00	91.00	11.00		0.7							
18b	H	40.6		11.0		0.00	890.00	88.00	11.00		1.1							-22.4
19a	H	33	4.46	11.0		0.00	859.00	119.00	11.00		0.5							
19b	H	33.2		15.0		0.00	874.00	101.00	10.00		0.6							-21.9
20a	H	30	0.14	3.10		0.00	916.00	70.00	10.90		0.5							
20b	H	37.5		5.60		0.00	921.37	61.02	12.00		0.5							-16.7
21a	H	30		2.90		0.00	888.09	97.01	12.00		0.5							
21b	H	31.8		3.50		0.00	902.45	83.04	11.01		0.5							-22.0
22a	H	35.1	3.30	2.30		0.00	874.74	109.97	13.00		0.6							
22b	H	25.5		2.50		0.00	887.44	98.05	12.01		0.6							-20.5
23a	H	37.7	21.5	81.0		0.08	903.01	3.70	12.00	0.01	45	4.1	19	4.7				
23b	H	29.2		152	0.50	0.25	840.00	0.33	6.90	0.08	260	29	4.7	15	32	3.0	2.1	-7.8
24a	H	33.1	28.0	15.0		0.02	894.98	79.00	11.00		16	1.5						
24b	H	26.9		69.00		0.14	918.04	1.80	11.00	0.02	120	16	2.4	78	22		0.6	-11.3
25a	H	41.3	9.78	15.00		0.01	890.99	83.00	11.00		2.8							
25b	H	38.5		26.00		0.02	910.98	52.00	11.00		9.1	1.1						-22.6

Table 3 continued

ID	Type	T	ΦCO ₂	CO ₂	H ₂ S	CH ₄	N ₂	O ₂	Ar	H ₂	C ₂ H ₆	C ₃ H ₈	n-C ₄ H ₁₀	i-C ₄ H ₈	C ₆ H ₆	C ₂ H ₆ S	C ₄ H ₄ S	δ ¹³ C-CO ₂
26a	H	35.8	3.59	3.20	0.00	0.00	865.83	119.98	11.00		0.6							-20.5
26b	H	33.3	5.50	5.50	0.00	0.00	888.44	95.05	11.01		0.5							
27a	H	27.3	15.4	7.30	0.20	0.01	859.42	122.06	11.01		4.1	0.5						
27b	H	27.8	22.3	12.01	0.30	0.02	887.60	89.06	11.01	0.03	15	1.7			1.1			-15.3
28a	H	27.7	22.3	21.99	0.04	0.04	874.79	91.98	11.00		19	2.2		1.2	2.5			
28b	H	30.1	22.7	39.02	0.05	0.05	923.51	25.01	12.01		26	3.3		1.5	4.7			-14.7
29a	H	27	22.7	25.00	0.03	0.03	863.98	100.00	11.00		17	1.5			1.3			
29b	H	27	22.7	39.00	0.05	0.05	930.96	18.00	12.00		35	3.9		2.5	3.8			-15.9
30a	H	25.9	2.17	11.00	0.01	0.01	848.99	129.00	11.00		3.8	0.5						
30b	H	26.9	13.01	13.01	0.02	0.02	874.86	101.10	11.01		8.5	0.9						-22.1
31a	H	23	2.21	5.40	0.01	0.01	842.65	141.94	10.00		2.1							
31b	H	21.9	9.60	9.60	0.01	0.01	861.33	118.05	11.00		3.8	0.5						-24.1
32a	H	26	1.59	4.10	0.01	0.01	854.91	129.99	11.00		1.5							
32b	H	23.9	5.30	5.30	0.01	0.01	888.73	94.97	11.00		3.7							-22.7
33a	H	33	14.9	31.03	0.04	0.04	871.83	86.08	11.01		21	2.1						
33b	H	33.6	65.99	65.99	0.11	0.11	905.90	16.00	12.00		78	8.8	1.3	5.6	5.1			-20.9
34a	H	34.3	0.75	2.10	0.00	0.00	838.91	147.98	11.00		1.1							
34b	H	34	2.20	2.20	0.00	0.00	841.83	144.97	11.00		1.5							-21.6
50a	B	27.7	0.43	4.10	0.00	0.00	844.91	139.99	11.00		1.9							
50b	B	26	4.50	4.50	0.01	0.01	866.43	118.06	11.01		2.4							-21.9
51a	B	30.5	0.23	4.60	0.00	0.00	861.34	123.05	11.00		1.5							
51b	B	27.8	4.50	4.50	0.00	0.00	889.44	95.05	11.01		1.4							-24.2

F fissure, C craters, V vegetation, H hydrothermalized, B blank

from 1.9 to 51 mmol/mol at 20 and 40 cm depth, respectively, in soil gases of type *V*, (3) from 2.1 to 81 mmol/mol and from 2.2 to 152 mmol/mol at 20 and 40 cm depth, respectively, in soil gases of type *H*, (4) from 11 to 841 mmol and from 19 to 411 mmol/mol at 20 and 40 cm depth, respectively, in soil gases of type *C*, and (3) ≤ 4.6 and ≤ 4.5 mmol/mol at 20 and 40 cm depth, respectively, in soil gases of type *B*. Methane contents (ranging from 0.001 to 2.30 mmol/mol and from 0.001 to 0.88 mmol/mol at 20 and 40 cm depth, respectively) increased at increasing CO₂, whereas O₂ (from 0.46 to 160 mmol/mol and from 0.11 to 145 mmol/mol at 20 and 40 cm depth) and Ar (from 0.91 to 13 mmol/mol and from 4.90 to 12 mmol/mol at 20 and 40 cm depth) showed an opposite behavior. H₂S (ranging from 0.1 to 37 mmol/mol and from 0.3 to 8.1 mmol/mol at 20 and 40 cm depth) and H₂ (from 0.01 to 0.69 mmol/mol and from 0.01 to 0.23 mmol/mol at 20 and 40 cm depth) were only detected in soil gases from *F*, *C*, and *H* sites. Among VOCs, ethane (C₂H₆) was the most abundant compound, with concentrations ranging from 0.5 to 2380 nmol/mol and from 0.5 to 1440 nmol/mol at 20 and 40 cm depth, respectively. Ethane was the only C₂₊ organic compound detected in gases from the *B* sites (≤ 2.4 nmol/mol), while in *V* sites it showed concentrations from 0.5 to 31 nmol/mol and characterized by the presence of propane (C₃H₈; ≤ 3.30 nmol/mol). The concentrations of C₂H₆ and C₃H₈ were markedly higher in *H* (up to 260 and 29 nmol/mol, respectively), *C* (up to 2380 and 270 nmol/mol, respectively) and *F* (up to 490 and 61 nmol/mol, respectively) sites, where normal-butane (*n*-C₄H₁₀; up to 4.70, 55 and 11 nmol/mol, respectively), iso-butene (*i*-C₄H₈; up to 78, 220, and 35 nmol/mol, respectively), benzene (C₆H₆; up to 32, 350 and 85 nmol/mol, respectively), dimethylsulfide (C₂H₆S; up to 3.00, 3.10, and 0.40 nmol/mol, respectively), and thiophene (C₄H₄S; up to 2.10, 19 and 2.60 nmol/mol, respectively) were also measured.

The $\delta^{13}\text{C}-\text{CO}_2$ values varied over a relatively wide range (Table 3). In soil gases from the *F* sites, they ranged from -17.1 to -2.5 ‰ vs. V-PDB. Similar values were measured in the *C* and *H* sites (from -23.8 to -0.9 ‰ vs. V-PDB and from -24.1 to -7.8 ‰ vs. V-PDB, respectively), whereas those in the soil gases from the *V* and *B* sites were ≤ -20.7 and ≤ -21.9 ‰ vs. V-PDB, respectively.

5.5 Chemical and isotopic composition of fumarolic gases

The chemical composition of the dry gas fraction of the fumaroles (Table 4) was dominated by CO₂ (from 784 to 905 mmol/mol) and H₂S (from 78 to 200 mmol/mol), with minor concentrations of CH₄ (from 1.8 to 9.8 mmol/mol) and H₂ (from 5.4 to 11 mmol/mol). The absence of detectable concentrations of strongly acidic gases and the outlet temperatures close to the boiling point of water (from 98.7 to 100.3 °C; Table 4) suggested that the fumarolic discharges are fed by boiling hydrothermal aquifers (Chiadini et al. 1993; Brombach et al. 2003). N₂, O₂, and Ar were present at relatively low concentrations (up to 2.9, 0.010 and 0.011 mmol/mol, respectively; Table 4).

VOCs mostly consisted of aromatics and alkanes, likely produced by thermogenic degradation of organic matter (Tassi et al. 2013; Fiebig et al. 2015), although abiotic processes were also invoked for CH₄ production (e.g., Fiebig et al. 2007, 2009). C₂H₆ and C₆H₆ were the most abundant species, with concentrations ranging from 2402 to 5128 nmol/mol and from 2016 to 4194 nmol/mol, respectively (Table 4). Minor amounts of C₃H₈ (from 343 to 730 nmol/mol), *i*-C₄H₈ (from 290 to 620 nmol/mol), and *n*-C₄H₁₀ (from 75 to 160 nmol/mol) were measured. C₂H₆S (from 2.50 to 7.90 nmol/mol) and C₄H₄S (from 5.12 to 17.2 nmol/mol) were also detected.

Table 4 Outlet temperature (in °C), chemical composition of the main gas species (CO₂, H₂S, CH₄, N₂, O₂, Ar, H₂; in mmol/mol) and volatile organic compounds (in nmol/mol) and δ¹³C–CO₂ values (in ‰ vs. V-PDB) in fumarolic gases from Phlegathon (Ph), Kaminakia (Kam), Stephanos (St1, St2), and Polybotes Micros (MicP) hydrothermal craters and Lofos dome (Lof)

ID	T	CO ₂	H ₂ S	CH ₄	N ₂	O ₂	Ar	H ₂	C ₂ H ₆	C ₃ H ₈	n-C ₄ H ₁₀	i-C ₄ H ₈	C ₆ H ₆	C ₂ H ₆ S	C ₄ H ₄ S	δ ¹³ C–CO ₂
Ph	99.5	856	134	1.8	2.9	0.0083	0.0064	5.8	4741	637	140	510	2375	6.90	15.0	– 1.1
Kam	98.7	905	78	9.8	1.8	0.0053	0.0053	5.4	2402	343	75	290	2016	2.50	5.12	– 1.4
St1	100.3	832	155	2.3	2.1	0.0057	0.011	7.9	5128	730	160	620	2603	4.80	9.86	– 1.1
St2	101.2	786	199	2.3	2.8	0.0095	0.0084	9.7	4735	681	150	560	2991	7.90	17.2	– 1.2
MicP	99.6	784	200	2.8	2.8	0.0082	0.011	11	3823	496	110	440	2159	6.10	14.1	– 1.0
Lof	99.4	828	162	2.9	2.4	0.010	0.011	5.4	2459	608	130	530	4194	5.80	15.7	– 1.3

The $\delta^{13}\text{C}\text{-CO}_2$ values ranged from -1.4 to -1.0 ‰ vs. V-PDB (Table 4), i.e., consistent with those reported in the literature (Kavouridis et al. 1999; Brombach et al. 2003), which were interpreted as related to thermometamorphic reactions on limestones hosting the deep hydrothermal aquifer.

6 Discussion

6.1 Evidences of hydrothermal alteration of the Lakki Plain soil

Hints on the trigger mechanism for the 2001–2002 collapse event can be inferred from the fissure orientation. Three trends (i.e., N030°, N070°, and N340°) were recognized, which closely resemble local tectonic lineaments (Volentik et al. 2005b), indicating a structural control on the location of the fissuring episode. Accordingly, the fissure is aligned with a fault that strikes the southern caldera wall (Vanderkluyzen and Gex 2005; Volentik et al. 2005b). Moreover, self-potential and VLF-tilt (very low-frequency) anomalies (Vanderkluyzen and Gex 2005) suggest that the fissure opened in an area possibly affected by intense fluid circulation. Fractures and faults are known to strongly control the hydrothermal fluid patterns in the subsurface of the Lakki Plain, as supported by the aligned location of the hydrothermal craters (Caliro et al. 2005; Tibaldi et al. 2008). Structural lineaments buried underneath the soft caldera deposits were also inferred on the basis of CO_2 soil flux anomalies recognized in the vegetated portion of the Lakki Plain (Caliro et al. 2005). These highly permeable lineaments are supposed to favor the uprising of hydrothermal fluids up to shallow depths (Gagliano et al. 2017). The interaction between the deep-originated fluids, highly aggressive due to the presence of acidic species (mainly CO_2 and H_2S), and the caldera-filling terrains is to be thought as a likely cause of hypogenic weathering (López and Williams 1993; Principe and Marini 2005; Daskalopoulou et al. 2014).

The occurrence of hydrothermal alteration on the loose, heterogeneous surficial materials filling the caldera in the fissure area can be assessed by evaluating the chemistry of the deposits exposed on the fissure walls (Fig. 3) with respect to that of the parent material. The latter was assumed to be represented by the lava flows and post-caldera dacitic-rhyolitic domes outcropping in the NW and SE portions of the caldera (i.e., Nikia and PCD units from Francalanci et al. 1995). The concentrations of selected major and trace elements were (1) normalized to primitive mantle (PM; Palme and O'Neill 2004) and compared to those of Nikia and PCD (Fig. 4a), (2) normalized to a selected immobile element (Al_2O_3) and expressed as enrichment factors (EF) relative to the parent material (Fig. 4b). The EF values for each element were calculated, as follows:

$$\text{EF}_i = \frac{(C_i/C_{\text{Al}_2\text{O}_3})_{\text{sample}}}{(C_i/C_{\text{Al}_2\text{O}_3})_{\text{parent}}}, \quad (3)$$

where $(C_i/C_{\text{Al}_2\text{O}_3})_{\text{sample}}$ and $(C_i/C_{\text{Al}_2\text{O}_3})_{\text{parent}}$ are the concentrations ratios of an element i normalized to Al_2O_3 in the sample and in the parent material, respectively. The computed EF values show that immobile elements, such as Ti, Fe, P, V, Ni, Sr, and Ba, are preferentially enriched with respect to volcanic rocks while mobile species, i.e., Na, Ca, K, Mn, and Rb are depleted (Fig. 4). This seems to confirm that the fissure wall deposits suffered leaching and weathering processes. The relatively high L.O.I. values (Table 2; Fig. 4b) in the fissure wall deposits are mainly related to structural water hosted by clay minerals,

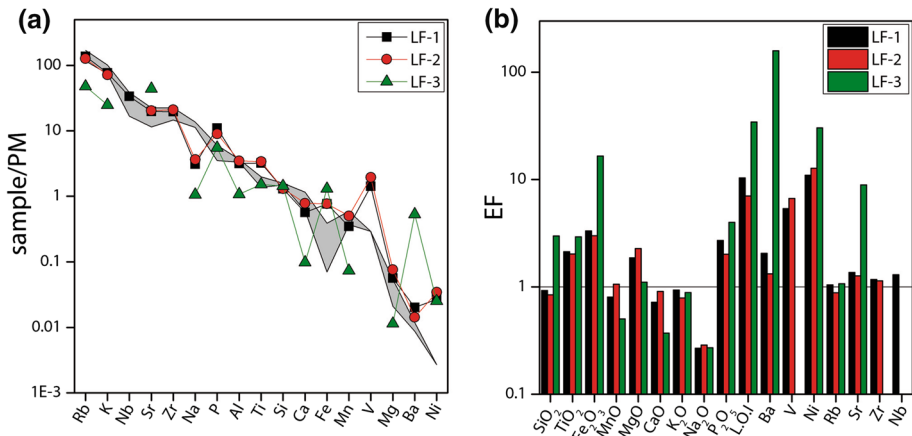


Fig. 4 **a** Primitive mantle (PM)-normalized element patterns for LF-1, LF-2, and LF-3 samples (normalization values are from Palme and O'Neill 2004) and **b** Enrichment factors for major and trace elements in fissure wall deposits relative to parent materials (see text for details). In **a**, PM-normalized concentrations of parent materials, i.e., Nikia and PCD rocks (according to Francalanci et al. 1995), are also reported (gray shaded area)

confirming intense alteration (argillification processes), as supported by the widespread presence of nontronite in the analyzed samples (Table 1). Accordingly, the XRD analyses revealed the occurrence of minerals typically related to advanced argillic alteration (AAA) assemblages characterizing steam-heated hydrothermal environments (Principe and Marini 2005; Zimbelman et al. 2005). Natroalunite and jarosite are generally formed by the dissolution of H_2S -bearing hydrothermal gases into ground waters followed by oxidation, driven by atmospheric O_2 , to sulfuric acid (Lueth et al. 2005; Principe and Marini 2005; Zimbelman et al. 2005), as follows:



A supply of H_2S or SO_4 -rich waters from hydrothermal fluid circulation was further confirmed by the strong enrichments in Ba and Sr in LF-3 (Fig. 4a, b), likely related to the formation of sulfate minerals. The presence of barite, which is typically related to the occurrence of mixing of hydrothermally derived SO_4 -rich solutions and dilute meteoric waters (Holland and Malinin 1979; Zimbelman et al. 2005), was recognized in the same sample. Furthermore, relatively high contents of S were measured in all the fissure wall deposits (Table 2), indicating the intense interaction between hydrothermal fluids and the caldera floor deposits, leading to acidic-sulfate leaching up to very shallow depths in the fissure area.

6.2 Past versus present hydrothermal fluid flow

While geochemical and mineralogical analyses on fissure wall deposits confirmed the fissure as an area of hydrothermal alteration, no information on whether hydrothermal fluid circulation in the fissure area is currently active can be provided. Soil temperature and diffuse CO_2 are important geochemical tools for evaluating heat and mass flow from hydrothermal reservoirs and identifying active faults and fractures acting as preferential pathways for the uprising gases (e.g., Giammanco et al. 1998; Toutain and Baubron 1999;

Chiodini et al. 2001, 2004; Viveiros et al. 2010). Accordingly, T and ΦCO_2 values were measured in the fissure bottom, as well as in the surroundings, to verify the presence of hydrothermal fluids at the surface. Previous studies, carried out before the collapse event (Brombach et al. 2001; Cardellini et al. 2003; Caliro et al. 2005), identified a CO_2 soil flux anomaly (with ΦCO_2 values up to $> 50 \text{ g m}^{-2} \text{ d}^{-1}$) in the fissure area, suggesting the presence of a buried NW–SE fault favoring the uprising of deep-sourced CO_2 -rich fluids towards the surface. Notwithstanding the expectations, no thermal or CO_2 flux anomalies were recognized in the present study (Figs. 5a; 6a), which was the first performed in the collapsed zone after the 2001–2002 event. The measured temperatures decreased at increasing depth, showing values comparable to those recorded in the background areas (V and B sites) and significantly lower than those measured in the hydrothermalized and crater areas (C and H sites) (Fig. 5b). On the other hand, the CO_2 soil fluxes within the fissure cannot clearly be distinguished with respect to those measured in the surrounding vegetated area (V sites), whereas they are significantly lower than those of the C sites that are evidently fed by deep hydrothermal fluids (Fig. 6a). This would imply that, on the basis of both soil temperatures and ΦCO_2 values, the fissure is currently not affected by hydrothermal fluid circulation. However, the strong variations of the ΦCO_2 values measured in the H sites (Table 3; Fig. 6a) are likely suggesting that hydrothermal alteration at the surface, which visibly characterizes these zones (Fig. 3), is able to significantly reduce the permeability of the topsoil (*self-sealing processes*, Facca and Tonani 1967), impeding upward gas migration and then producing gas accumulation in the soil. Accordingly, interstitial soil gas chemistry, which is a reliable tool to trace active tectonic structures and ascending deep gases (e.g., Ciotoli et al. 1998; Baubron et al. 2002; Aiuppa et al. 2004; Fu et al. 2005; Han et al. 2014), was used to verify the occurrence of a similar scenario in the fissure.

As shown in Fig. 6b, the relatively high CO_2 concentrations measured in the interstitial soil gases from the fissure bottom, despite their low CO_2 soil fluxes (Fig. 6a), were comparable to those in C gases and even higher than those measured in H. Similarly, with

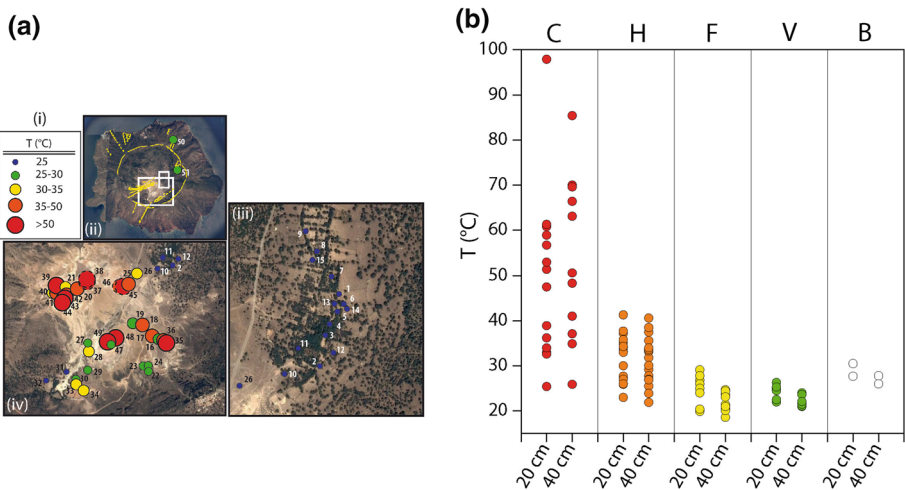


Fig. 5 **a** Dot map of soil temperatures (°C) at 40 cm depths (dash countered circles: soil temperatures at 20 cm depth) in the study area. **b** Soil temperature (°C) measured at 20 and 40 cm depths in C, H, F, V and B sites (symbols as in Fig. 1)

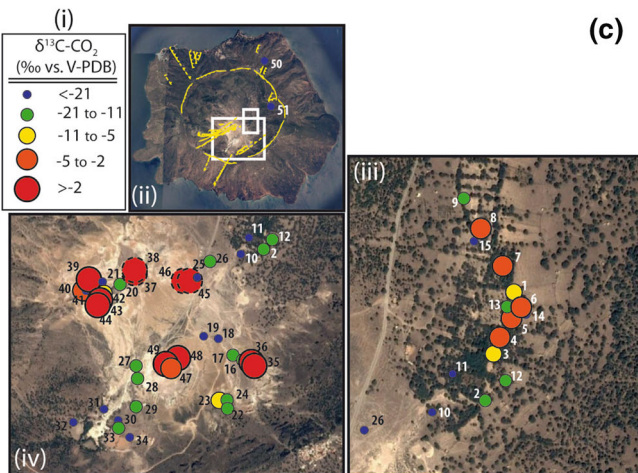
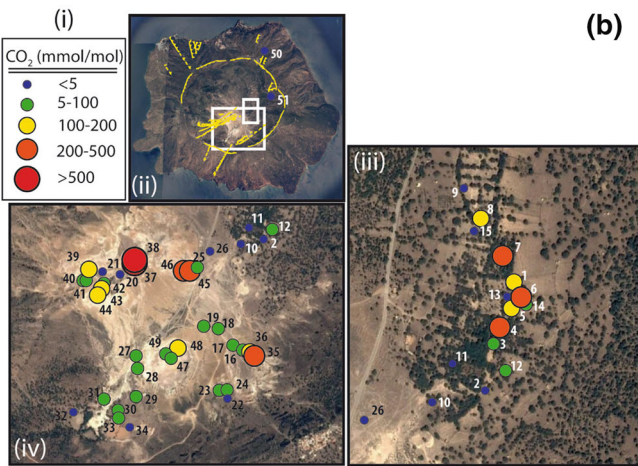
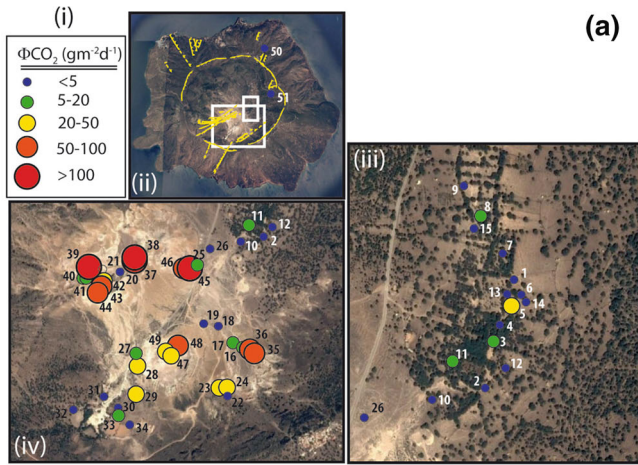


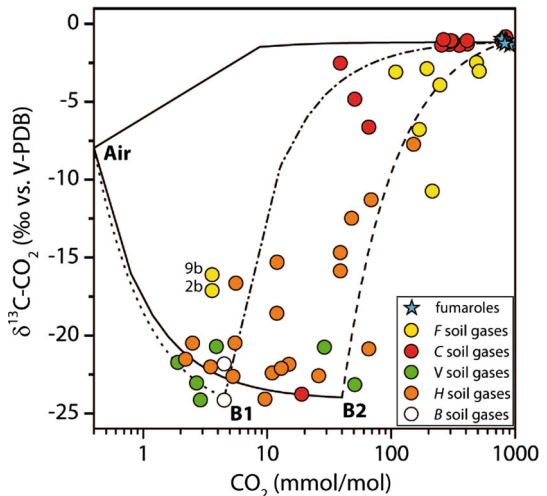
Fig. 6 Dot maps of **a** ΦCO_2 values (in $\text{g m}^{-2} \text{day}^{-1}$), **b** CO_2 concentrations (in mmol/mol) in soil gases at 20 cm depth and **c** $\delta^{13}\text{C}\text{-CO}_2$ values (in ‰ vs. V-PDB) in soil gases at 40 cm depth (dash countered circles: soil gases at 20 cm depth) in the study area

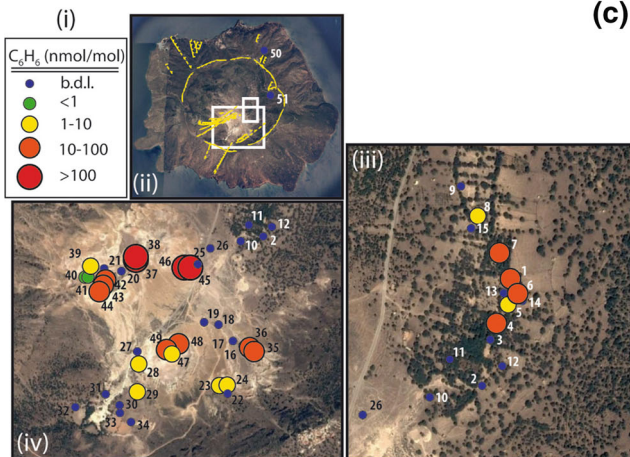
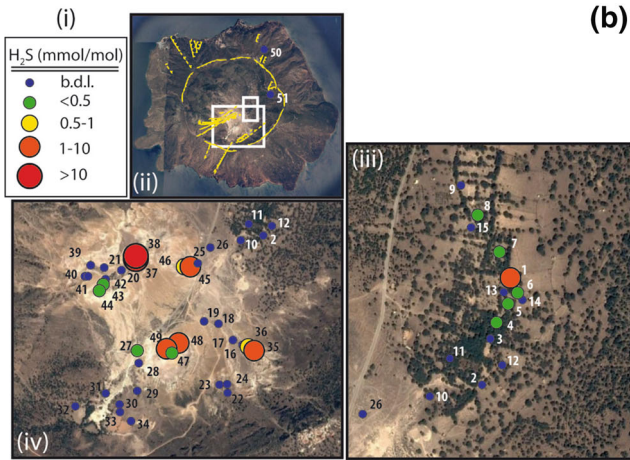
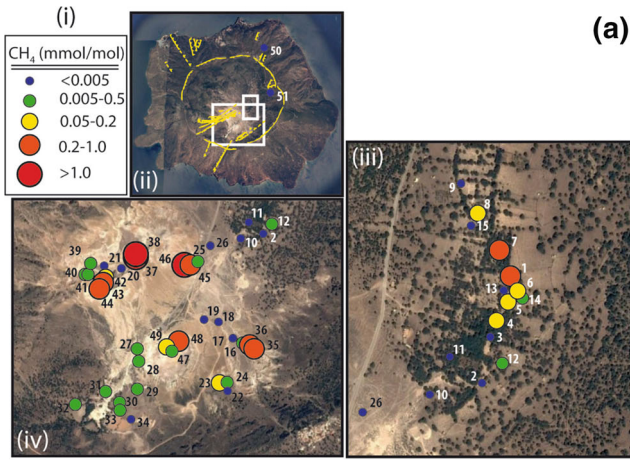
the only exception of two samples (#2b and #9b), which were characterized by relatively high O_2 and Ar concentrations, indicating a strong air contamination, the *F* interstitial soil gases showed markedly higher $\delta^{13}\text{C}\text{-CO}_2$ values with respect to those measured in the *V* and *B* gases and comparable with those measured in *C* gases (Figs. 6c; 7).

To investigate the source of such amounts of CO_2 , the $\delta^{13}\text{C}\text{-CO}_2$ values measured in the interstitial soil gases at 40 cm depth in the whole study area were plotted versus CO_2 concentrations (Fig. 7). The different curves in Fig. 7 represent different mixing trends of the hydrothermal end-member, i.e., the average CO_2 concentration and $\delta^{13}\text{C}\text{-CO}_2$ value of the fumarolic gas samples (832 mmol/mol and -1.2 ‰ vs. V-PDB, respectively), with (1) air (CO_2 and $\delta^{13}\text{C}\text{-CO}_2$: 0.400 mmol/mol and -8.0 ‰ versus V-PDB, respectively; solid curve), (2) a CO_2 -poor biogenic end-member (B1; CO_2 and $\delta^{13}\text{C}\text{-CO}_2$: 4.5 mmol/mol and -24 ‰ vs. V-PDB, respectively; dash dot curve), and (3) a CO_2 -rich biogenic end-member (B2; CO_2 and $\delta^{13}\text{C}\text{-CO}_2$: 40 mmol/mol and -24 ‰ vs. V-PDB, respectively; dash curve), where B1 and B2 refer to different conditions of vegetation cover, microbial decomposition of soil organic matter and soil characteristics, including soil permeability. The *V*, *B* and, in part, *H* interstitial soil gases plot close to the biogenic end-members and along the mixing lines between air and B1 and B2, respectively, indicating a shallow source of CO_2 . Differently, both *C* and *F* gases (with few exceptions), and *H* gases with $\delta^{13}\text{C}\text{-CO}_2$ values ≥ -20 ‰ vs. V-PDB, are aligned along the mixing lines between the biogenic end-members and the fumarolic gases, suggesting the occurrence of a supply of hydrothermal fluids beneath the fissure.

Accordingly, the typical hydrothermal gases (H_2S , H_2 , CH_4) (Table 4) were detected in *F* samples at concentrations markedly higher than those measured in *V* sites (Table 3; Fig. 8a, b), indicating the occurrence of active hydrothermal fluid circulation underneath the fissure. The latter was further confirmed by the presence of VOCs, typically related to hydrothermal fluids (e.g., ethane, propane, benzene, and S-bearing compounds; Table 1; Fig. 8c), in *F* soil gases at concentrations orders of magnitude higher than those measured

Fig. 7 $\delta^{13}\text{C}\text{-CO}_2$ values (in ‰ vs. V-PDB) vs. CO_2 concentrations (in mmol/mol) in soil gases at 40 cm depth and fumarolic emissions. Symbols as in Fig. 1. Mixing lines between i hydrothermal, ii air, iii CO_2 -poor biogenic (B1), and iv a CO_2 -rich biogenic (B2) end-members are also reported





◀ **Fig. 8** Dot maps of **a** CH₄ and **b** H₂S concentrations (in mmol/mol), and **c** C₆H₆ contents (in nmol/mol) in soil gases at 20 cm depth in the study area

in *B* and *V* sites and comparable to those observed in *H* and *C* sites. In particular, the presence of DMS and thiophenes, which are considered to be quite readily affected by secondary degradation processes during the migration of deep-derived fluids at shallow depths (Tassi et al. 2015), in *F* soil gases are indicative of a relatively rapid ascent of reduced gases from the hydrothermal reservoir to the fissure.

7 Conclusions

Results of mineralogical and chemical analyses on the 2001–2002 fissure wall deposits in the Lakki Plain evidenced the occurrence of hydrothermal alteration caused by acidic fluids at shallow depths. Although no thermal or CO₂ soil flux anomalies were identified, both chemical and isotopic evidences on interstitial soil gases collected from the fissure bottom revealed that hydrothermal fluids currently circulate underneath the vegetated portion of the Lakki Plain. These acidic fluids, which are conveyed along structural lineaments, probably reactivated after the 1996–1998 seismic crisis, have softened and weakened the caldera deposits, causing the 2001–2002 fissuring episode, and might trigger further collapse events, either extending the 2001–2002 fissure or producing new events along identified or still unknown buried faults and fractures.

The possibility that further sudden ground collapses in the Lakki central plain area may occur in the future is matter of evident concern on an island that is visited by several hundreds of tourists per day during the summertime. This calls for increasing monitoring efforts. Detailed collapse risk assessment and mapping for Lakki Plain can be achieved combining (1) structural information, (2) geochemical and mineralogical investigations on conditions of alteration of caldera-filling terrains, (3) soil temperature and diffuse CO₂ degassing measurements, and (4) extensive periodical sampling campaigns of interstitial soil gases throughout the caldera floor. The recognition of buried lineaments and shallow hydrothermal fluid pathways would allow the delimitation of areas of future potential collapse episodes and the identification of weaknesses in a volcanic-hydrothermal system where a strict connection between structural settings and phreatic explosions has been recognized.

Although fissure collapses similar to that occurred at Nisyros in 2001–2002 are not very common, collapse risks do indeed exist in any volcanic-hydrothermal system characterized by acidic fluid circulation at shallow depths. Even if collapses usually occur at local scale, they are sudden and often without any precursory signs. The main risks for the population may thus be associated with panicking unless buildings and infrastructures are involved in the trajectory as the fissure proceeds. The collapse-related hazard would then be even sharpened in calderas affected by intense urbanization, such as Campi Flegrei (southern Italy), thereby requiring special efforts aimed at identifying areas of hydrothermal fluid flow that are most vulnerable to collapse episodes and developing prevention initiatives and risk mitigation strategies.

Acknowledgements This work was financially supported by a project between IGME-Athens and the Department of Earth Sciences of Florence, the laboratories of Fluid and Rock Geochemistry and Stable Isotope Geochemistry (Department of Earth Sciences of Florence) and the Institute of Geosciences and Earth Resources of the National Research Council of Italy (IGG-CNR Florence). Part of this work was presented as an oral contribution at the EGU General Assembly 2016 (Venturi et al. 2016). E. Calvi (CNR-IGG Pisa), E. Pecchioni (Department of Earth Sciences of Florence) and S. Ciattini (CRIST Florence) are warmly thanked for

their help for the IRMS, XRD and XRF analysis, respectively. Many thanks are due to A. Gallorini and A. Raspani for their help during the sampling campaign. The authors wish to thank two anonymous reviewers for their helpful comments that contributed to improve the first version of the manuscript.

References

- Aiuppa A, Caleca A, Federico C, Gurrieri S, Valenza M (2004) Diffuse degassing of carbon dioxide at Somma–Vesuvius volcanic complex (Southern Italy) and its relation with regional tectonics. *J Volcanol Geotherm Res* 133:55–79
- Ambrosio M, Doveri M, Fagioli MT, Marini L, Principe C, Raco B (2010) Water-rock interaction in the magmatic-hydrothermal system of Nisyros Island (Greece). *J Volcanol Geotherm Res* 192:57–68
- Arthur CL, Pawliszyn J (1990) Solid phase microextraction with thermal desorption using fused silica optical fibers. *Anal Chem* 62(19):2145–2148
- Baubron JC, Rigo A, Toutain JP (2002) Soil gas profiles as a tool to characterise active tectonic areas: the Jaut Pass example (Pyrenees, France). *Earth Planet Sci Lett* 196:69–81
- Billi A, De Filippis L, Poncia PP, Sella P, Faccenna C (2016) Hidden sinkholes and karst cavities in the travertine plateau of a highly-populated geothermal seismic territory (Tivoli, central Italy). *Geomorphology* 255:63–80
- Bosák P (2000) Notes on the history of some karstological terms—hydrothermal karst, geysermite, vadose zone. *Acta Carsol* 29:233–240
- Brombach T, Hunziker JC, Chiodini G, Cardellini C, Marini L (2001) Soil diffuse degassing and thermal energy fluxes from the southern Lakki plain, Nisyros (Greece). *Geophys Res Lett* 28(1):69–72
- Brombach T, Caliro S, Chiodini G, Fiebig J, Hunziker JC, Raco B (2003) Geochemical evidence for mixing of magmatic fluids with seawater, Nisyros hydrothermal system, Greece. *Bull Volcanol* 65:505–516
- Caliro S, Chiodini G, Galluzzo D, Granieri D, La Rocca M, Saccorotti G, Ventura G (2005) Recent activity of Nisyros volcano (Greece) inferred from structural, geochemical and seismological data. *Bull Volcanol* 67:358–369
- Caramanna G, Ciotoli G, Nisio S (2008) A review of natural sinkhole phenomena in Italian plain areas. *Nat Hazards* 45:145–172
- Cardellini C, Chiodini G, Frondini F, Granieri D, Lewicki J, Peruzzi L (2003) Accumulation chamber measurements of methane fluxes: application to volcanic-geothermal areas and landfills. *Appl Geochem* 18:45–54
- Chiodini G, Cioni R, Leonis C, Marini L, Raco B (1993) Fluid geochemistry of Nisyros island, Dodecanese, Greece. *J Volcanol Geotherm Res* 56(1–2):95–112
- Chiodini G, Cioni R, Guidi M, Raco B, Marini L (1998) Soil CO₂ flux measurements in volcanic and geothermal areas. *Appl Geochem* 13(5):543–552
- Chiodini G, Frondini F, Cardellini C, Granieri D, Marini L, Ventura G (2001) CO₂ degassing and energy release at Solfatara volcano, Campi Flegrei, Italy. *J Geophys Res* 106(B8):16213–16221
- Chiodini G, Brombach T, Caliro S, Cardellini C, Marini L, Dietrich V (2002) Geochemical indicators of possible ongoing volcanic unrest at Nisyros Island (Greece). *Geophys Res Lett* 29(16):1759
- Chiodini G, Avino R, Brombach T, Caliro S, Cardellini C, De Vita S, Frondini F, Granieri D, Marotta E, Ventura G (2004) Fumarolic and diffuse soil degassing west of Mount Epomeo, Ischia, Italy. *J Volcanol Geotherm Res* 133:291–309
- Ciotoli G, Guerra M, Lombardi S, Vittori E (1998) Soil gas survey for tracing seismogenic faults: a case study in the Fucino basin, Central Italy. *J Geophys Res* 103(B10):23781–23794
- Daskalopoulou K, Calabrese S, Milazzo S, Brusca L, Bellomo S, D’Alessandro W, Kyriakopoulos K, Tassi F, Parello F (2014) Trace elements mobility in soils from the hydrothermal area of Nisyros (Greece). *Ann Geophys* 57(Fast Track 2):1–6
- Dublyansky YV (2000) Hydrothermal speleogenesis—its settings and peculiar features. In: Klimchouk AB, Ford DC, Palmer AN, Dreybrodt W (eds) *Speleogenesis: evolution of karst aquifers*. National Speleological Society, Huntsville, pp 292–297
- Dublyansky YV (2013) Karstification by geothermal waters. In: Shroder JF (ed) *Treatise on geomorphology*, vol 6. Academic Press, San Diego, pp 57–71
- Evans WC, White LD, Rapp JB (1998) Geochemistry of some gases in hydrothermal fluids from the southern Juan de Fuca ridge. *J Geophys Res* 15:305–313
- Facca G, Tonani F (1967) The self-sealing geothermal field. *Bull Volcanol* 30(1):271–273
- Fiebig J, Woodland AB, Spangenberg J, Oschmann W (2007) Natural evidence for rapid abiogenic hydrothermal generation of CH₄. *Geochim Cosmochim Acta* 71:3028–3039

- Fiebig J, Woodland AB, D'Alessandro W, Püttmann W (2009) Excess methane in continental hydrothermal emissions is abiogenic. *Geology* 37(6):495–498
- Fiebig J, Hofmann S, Tassi F, D'Alessandro W, Vaselli O, Woodland AB (2015) Isotopic patterns of hydrothermal hydrocarbons emitted from Mediterranean volcanoes. *Chem Geol* 396:152–163
- Françalanci L, Varekamp JC, Vougioukalakis G, Defant MJ, Innocenti F, Manetti P (1995) Crystal retention, fractionation and crystal assimilation in a convecting magma chamber, Nisyros Volcano, Greece. *Bull Volcanol* 56:601–620
- Françalanci L, Vougioukalakis GE, Perini G, Manetti P (2005) A west-east traverse along the magmatism of the south Aegean volcanic arc in the light of volcanological, chemical and isotope data. In: Fytikas M, Vougioukalakis GE (eds) *The South Aegean active volcanic arc, present knowledge and future perspectives*. Developments in volcanology, vol 7. Elsevier, Amsterdam, pp 65–111
- Frumkin A, Zaidner Y, Na'aman I, Tsatskin A, Porat N, Vulfson L (2015) Sagging and collapse sinkholes over hypogenic hydrothermal karst in a carbonate terrain. *Geomorphology* 229:45–57
- Fu CC, Yang TF, Walia V, Chen CH (2005) Reconnaissance of soil gas composition over the buried fault and fracture in southern Taiwan. *Geochem J* 39:427–439
- Gagliano AL, Calabrese S, Daskalopoulou K, Cabassi J, Capecciacci F, Tassi F, Bonsignore M, Sprovieri M, Kyriakopoulos K, Bellomo S, Brusca L, D'Alessandro W (2017) Mobility of mercury in the volcanic/geothermal area of Nisyros (Greece). *Bull Geol Soc Greece* 50:2118–2126
- Geotermica Italiana (1983) Nisyros 1 geothermal well. Unpublished PPC-EEC report, p 106
- Geotermica Italiana (1984) Nisyros 2 geothermal well. Unpublished PPC-EEC report, p 44
- Giammanco S, Gurrieri S, Valenza M (1998) Anomalous soil CO₂ degassing in relation to faults and eruptive fissures on Mount Etna (Sicily, Italy). *Bull Volcanol* 60:252–259
- Gutiérrez F, Parise M, De Waele J, Jourde H (2014) A review on natural and human-induced geohazards and impacts in karst. *Earth Sci Rev* 138:61–88
- Han X, Li Y, Du J, Zhou X, Xie C, Zhang W (2014) Rn and CO₂ geochemistry of soil gas across the active fault zones in the capital area of China. *Nat Hazards Earth Syst Sci* 2:1729–1757
- Heidari M, Khanlari GR, Taleb Beydokhti AR, Momeni AA (2011) The formation of cover collapse sinkholes in North of Hamedan, Iran. *Geomorphology* 132:76–86
- Holland HD, Malinin SD (1979) The solubility and occurrence of non-ore minerals. In: Barnes HL (ed) *Geochemistry of hydrothermal ore deposits*, 2nd edn. Wiley, New York, pp 461–508
- Hurni L, Jenny B, Gogu R, Freimark H, Terribilini A, Dietrich V (2005) Geowarn: a web-based atlas information system for volcanic monitoring. In: Proceedings of the 21st international cartographic conference ICC 2005, A Coruña, Spain
- Kavouridis T, Kuris D, Leonis C, Liberopoulou V, Leontiadis J, Panichi C, La Ruffa G, Caprai A (1999) Isotope and chemical studies for a geothermal assessment of the island of Nisyros (Greece). *Geothermics* 28(2):219–239
- Kinzig HS, Winson A, Gottsmann J (2010) Analysis of volcanic threat from Nisyros Island, Greece, with implications for aviation and population exposure. *Nat Hazards Earth Syst Sci* 10:1101–1113
- Lagios E, Sakkas V, Is Parcharidis, Dietrich V (2005) Ground deformation of Nisyros Volcano (Greece) for the period 1995–2002: results from DInSAR and DGPS observations. *Bull Volcanol* 68:201–214
- Linares R, Roqué C, Gutiérrez F, Zarroca M, Carbonel D, Bach J, Fabregat I (2017) The impact of droughts and climate change on sinkhole occurrence. A case study from the evaporite karst of the Fluvia Valley, NE Spain. *Sci Total Environ* 579:345–358
- López DL, Williams SN (1993) Catastrophic volcanic collapse: relation to hydrothermal processes. *Science* 260:1794–1796
- Lueth VW, Rye RO, Peters L (2005) “Sour gas” hydrothermal jarosite: ancient to modern acid-sulfate mineralization in the southern Rio Grande Rift. *Chem Geol* 215:33–360
- Marini L, Fiebig J (2005) Fluid geochemistry of the magmatic-hydrothermal system of Nisyros (Greece). In: Hunziker JC, Marini L (eds) *The geology, geochemistry and evolution of Nisyros Volcano (Greece), implications for the volcanic hazards*. *Memoires de Geologie, Lausanne*, pp 121–163
- Marini L, Principe C, Chiodini G, Cioni R, Fytikas M, Marinelli G (1993) Hydrothermal eruptions of Nisyros (Dodecanese, Greece). Past events and present hazard. *J Volcanol Geotherm Res* 56:71–94
- Montegrossi G, Tassi F, Vaselli O, Buccianti A, Garofalo K (2001) Sulphur species in volcanic gases. *Anal Chem* 73:3709–3715
- Palme H, O'Neill HStC (2004) Cosmochemical estimates of mantle composition. In: Holland HD, Turekian KK (eds) *Treatise on geochemistry*, vol 2. Elsevier, Amsterdam, pp 1–38
- Papadopoulos GA, Sachpazi M, Panopoulou G, Stavrakakis G (1998) The volcanoseismic crisis of 1996–97 in Nisyros, SE Aegean Sea, Greece. *Terra Nova* 10(3):151–154
- Pe-Piper G, Piper DJW (2005) The South Aegean active volcanic arc: relationships between magmatism and tectonics. In: Fytikas M, Vougioukalakis GE (eds) *The South Aegean active volcanic arc, present*

- knowledge and future perspectives. *Developments in volcanology*, vol 7. Elsevier, Amsterdam, pp 113–133
- Principe C, Marini L (2005) Reaction path modeling of argillic alteration (AA) and advanced argillic alteration (AAA): consequences for debris avalanches induced by flank collapse and hydrothermal eruptions. In: Hunziker JC, Marini L (eds) *The geology, geochemistry and evolution of Nisyros Volcano (Greece)*, implications for the volcanic hazards, vol 44. *Memoires de Geologie, Lausanne*, pp 164–182
- Rosas-Carbajal M, Komorowski JC, Nicollin F, Gilbert D (2016) Volcano electrical tomography unveils edifice collapse hazard linked to hydrothermal system structure and dynamics. *Sci Rep* 6:29899
- Santo A, Ascione A, Del Prete S, Di Crescenzo G, Santangelo N (2011) Collapse sinkholes distribution in the carbonate massifs of central and southern Apennines. *Acta Carsol* 40:95–112
- Tassi F, Capecchiacci F, Buccianti A, Vaselli O (2012) Sampling and analytical procedures for the determination of VOCs released into air from natural and anthropogenic sources: a comparison between SPME (solid phase micro extraction) and ST (solid trap) methods. *Appl Geochem* 27:115–123
- Tassi F, Capecchiacci F, Giannini L, Vougioukalakis GE, Vaselli O (2013) Volatile organic compounds (VOCs) in air from Nisyros Island (Dodecanese Archipelago, Greece): natural versus anthropogenic sources. *Environ Pollut* 180:111–121
- Tassi F, Venturi S, Cabassi J, Capecchiacci F, Nisi B, Vaselli O (2015) Volatile organic compounds (VOCs) in soil gases from Solfatara crater (Campi Flegrei, southern Italy): geogenic source(s) vs. biogeochemical processes. *Appl Geochem* 56:37–49
- Tibaldi A, Pasquarè FA, Papanikolaou D, Nomikou P (2008) Tectonics of Nisyros Island, Greece, by field and offshore data, and analogue modelling. *J Struct Geol* 30:1489–1506
- Toutain JP, Baubron JC (1999) Gas geochemistry and seismotectonics: a review. *Tectonophysics* 304:1–27
- Vanderkluyzen L, Gex P (2005) A geochemical investigation of Nisyros' hydrothermal field using the self-potential and very low frequencies-tilt methods. In: Hunziker JC, Marini L (eds) *The geology, geochemistry and evolution of Nisyros Volcano (Greece)*, Implications for the volcanic hazards, vol 44. *Memoires de Geologie, Lausanne*, pp 107–114
- Vanderkluyzen L, Volentik A, Hernandez J, Hunziker JC, Bussy F, Principe C (2005) The petrology and geochemistry of lavas and tephra of Nisyros Volcano (Greece). In: Hunziker JC, Marini L (eds) *The geology, geochemistry and evolution of Nisyros Volcano (Greece)*, implications for the volcanic hazards, vol 44. *Memoires de Geologie, Lausanne*, pp 79–99
- Vaselli O, Tassi F, Montegrossi G, Capaccioni B, Giannini L (2006) Sampling and analysis of volcanic gases. *Acta Vulcanol* 18(1–2):65–76
- Venturi S, Tassi F, Kanellopoulos C, Vaselli O, Caponi C, Ricci A, Raspanti A, Gallorini A, Cabassi J, Vougioukalakis GE (2016) Soil gas composition from the 2001–2002 fissure in the Lakki Plain (Nisyros Island, Greece): evidences for shallow hydrothermal fluid circulation. *EGU General Assembly 2016, Vienna, Austria*; 17–22 April 2016
- Viveiros F, Cardellini C, Ferreira T, Caliro S, Chiodini G, Silva C (2010) Soil CO₂ emissions at Furnas volcano, São Miguel Island, Azores archipelago: volcano monitoring perspectives, geomorphologic studies, and land use planning application. *J Geophys Res* 115:B12208
- Volentik A, Principe C, Vanderkluyzen L, Hunziker JC (2005a) Explanatory notes on the “Geological Map of Nisyros Volcano (Greece)”. In: Hunziker JC, Marini L (eds) *The geology, geochemistry and evolution of Nisyros Volcano (Greece)*, implications for the volcanic hazards, vol 44. *Memoires de Geologie, Lausanne*, pp 7–25
- Volentik ACM, Vanderkluyzen L, Principe C, Hunziker JC (2005b) The role of tectonic and volcano-tectonic activity at Nisyros Volcano (Greece). In: Hunziker JC, Marini L (eds) *The geology, geochemistry and evolution of Nisyros Volcano (Greece)*, implications for the volcanic hazards, vol 44. *Memoires de Geologie, Lausanne*, pp 67–78
- Vougioukalakis GE (2003) Passive fissuring in long-dormant caldera volcanoes: the Nisyros case. Meeting on “The South Aegean Volcanic Arc: Present knowledge and future perspectives”, Milos island, Greece. *Book of abstracts* 105
- Vougioukalakis GE, Fytikas M (2005) Volcanic hazards in the Aegean area, relative risk evaluation, monitoring and present state of the active volcanic centers. In: Fytikas M, Vougioukalakis GE (eds) *The South Aegean active volcanic arc, present knowledge and future perspectives. Developments in volcanology*, vol 7. Elsevier, Amsterdam, pp 161–183
- Waltham T, Fookes PG (2003) Engineering classification of karst ground conditions. *Q J Eng Geol Hydrogeol* 36(2):101–118
- Waltham T, Bell F, Culshaw M (2005) Sinkholes and subsidence. *Karst and cavernous rocks in engineering and construction*. Springer, Berlin
- Zimbelman DR, Rye RO, Breit GN (2005) Origin of secondary sulfate minerals on active andesitic stratovolcanoes. *Chem Geol* 215:37–60